Astronomy & Astrophysics

Monitoring of asteroids in cometary orbits and activated asteroids through archival images and new observations[*]

S. Martino[1],[**] , G. Tancredi[1], M. Banda-Huarca[2,3], E. Rondón[2] , J. I. B. Camargo[2,3] , J. Licandro[4], M. Aguena[3],
F. Andrade-Oliveira[5], P. Arcoverde[2], P. H. Bernardinelli[6], D. Brooks[7], A. Carnero Rosell[3,4] , J. Carretero[8] ,
L. N. da Costa[3], T. M. Davis[9], J. De Vicente[10] , H. T. Diehl[11], P. Doel[7], M. Evangelista-Santana[2] , S. Everett[12],
J. Frieman[11], J. García-Bellido[13] , E. Gaztanaga[14,15], D. Gruen[16] , R. A. Gruendl[17] , S. R. Hinton[9],
D. L. Hollowood[18], D. J. James[19], K. Kuehn[20], O. Lahav[7], J. L. Marshall[21], H. Medeiros[2], J. Mena-Fernández[22] ,
F. W. Mesquita[2], J. Michimani[2] , R. Miquel[8], F. Monteiro[2] , J. W. Pereira[2] , A. Pieres[3] ,
A. A. Plazas Malagón[23,24] , S. Samuroff[8,25], E. Sanchez[10] , D. Sanchez Cid[10], I. Sevilla-Noarbe[10],
M. Smith[26], E. Suchyta[27], G. Tarle[28], and N. Weaverdyck[29,30]

(Affiliations can be found after the references)

ABSTRACT

Context. Transitional objects are minor bodies that share some characteristics with asteroids and others with comets. These objects include asteroids in cometary orbits (ACOs), which behave dynamically like comets, but lack observed activity, while activated asteroids (AAs) follow typical asteroidal orbits, but have shown dust ejections.

Aims. The monitoring of a set of these objects carried out in 2015 and 2016 is continued using archival images from various observatories and new data from the IMPACTON telescope in Brazil.

Methods. Two techniques were applied to detect activity: (i) surface brightness profiles were compared with those of field stars to identify widening, and (ii) the magnitudes reported in the Minor Planet Center, combined with our observations, were reduced and analyzed to identify abrupt brightness increases as a function of heliocentric distance.

Results. We analyzed the surface brightness profiles of 133 ACOs and 7 AAs. To study the reduced magnitude, we obtained data from the 705 ACOs that were known at the time of the analysis. Together with the data from our previous work, our analysis covered 23% of the total known ACOs; 8 deviated slightly in the surface brightness profile, 6 brightened in the reduced magnitude, and one object is in common in both samples. A very low percentage of objects might show activity (4% of the sample with brightness profiles and <1% in the reduced magnitudes). These results would rule out a slow transition from active to inert. Regarding AAs, 4 showed activity, and 3 of them matched previously reported periods, while the data we analyzed for P/2015 X_6 were obtained 19 days before the first existing activity report. The activity episodes of these objects are very restricted in time and do not always occur in the same region of the orbit.

Key words. comets: general – minor planets, asteroids: general

1. Introduction

The study of asteroids and comets has always been especially relevant because they are the remnants of the formation of the Solar System, and their physical and chemical properties have remained practically unchanged since their origins. When we analyze them, we may also be able to determine the conditions required for our planetary system to form, and its subsequent evolution.

Asteroids are rocky objects with nonexistent or negligible volatile substances, and they appear as inert bodies, whose brightness variations are solely attributed to rotational factors. Comets have a substantial ice content on their surface and interior, observationally have a coma, and can show one or more tails. However, comets do not show activity during their entire orbit, but do so when they approach the Sun. Even then, the detection of a coma or tail is contingent upon the prevailing observability conditions and the sensitivity of the instruments used. This introduces the possibility that objects with very low activity go unnoticed by the instruments that perform the observation if the instruments are not sensitive enough.

Tisserand's parameter (Kresak 1979) has been fundamental for the historical classification of objects into asteroids and comets. The parameter arises from the restricted three-body problem. From the Jacobi integral, we can derive the Tisserand parameter, given by Eq. (1), where a_p is the semimajor axis of the planet in circular orbit around the Sun, and a, e, and i are the semimajor axis, eccentricity, and inclination of the particle, respectively,

$$T_p = \frac{a_p}{a} + 2\sqrt{\frac{a}{a_p}(1-e^2)}\cos(i). \qquad (1)$$

A purely dynamic criterion is to consider asteroids as objects with $T_{Jup} > 3$ and comets as objects with $T_{Jup} < 3$. However, this simple criterion has been questioned, and further

refinements are necessary to achieve a proper classification scheme between these populations (see, e.g., Tancredi 2014).

As increasingly more objects were discovered, the categories that were traditionally used to classify them began to be insufficient. We commonly speak of "transitional objects" to refer to objects that do not fully fit one of the traditional categories. Hsieh (2017) called them "continuum objects", in relation to the fact that there is no clear line that distinguishes them. We analyze two populations of transitional objects and refer to them as asteroids in cometary orbits (ACOs) and activated asteroids (AAs). We follow the clasification scheme presented by Tancredi (2014).

An ACO is an object whose orbit has a moderate to high inclination and eccentricity, with a low relative encounter velocity with Jupiter. It therefore belongs to an unstable population, similar to the Jupiter-family comets (JFCs), whose dynamic lives are about 10^4–10^5 years (see, e.g., Alvarez-Candal & Roig 2005 and Di Sisto et al. 2009).

Several physical studies (albedo determination, spectrum analysis, etc.) of ACOs have been carried out in the past decade, such as the works of Alvarez-Candal (2013), Kim et al. (2014), Licandro et al. (2016), Licandro et al. (2018), Simion et al. (2020), and Geem et al. (2022). From these works, it can be deduced that a high percentage of the studied objects are observationally compatible with cometary nuclei; that is, their albedos, colors, and spectra are similar. Some dynamic studies have also been carried out, among which we highlight the work of Hsieh & Haghighipour (2016). They showed that some objects with initial JFC orbits can evolve into orbits of main-belt asteroids on relatively short timescales (<2 Myr), and vice versa. Ye et al. (2016) also carried out dynamical studies on a large set of ACOs in the population of near-Earth asteroids (NEAs). They reported a lower limit of 2% dormant comets in the near-Earth object (NEO) population. However, the results reported by different authors must be compared with caution because varying criteria may have been used to classify an object within the ACOs population.

Moreover, activity has been observed in bodies that do not follow cometary orbits. Objects in the main asteroid belt were assumed to be inactive for a long time because it was thought that any volatiles they might have had sublimated during their lifetime. This concept was challenged, however, by the discovery of objects that were at first known as main-belt comets and later as active asteroids (Elst et al. 1996, Hsieh et al. 2004, and Hsieh & Jewitt 2006). Since then, a few dozen of these objects have been discovered (Chandler et al. 2024).

We will use the term 'activated' in this paper to refer to objects that exhibit a dynamic behavior similar to that of asteroids (regardless of whether they belong to the main belt) and that showed one or several episodes of activation in the past, that is, a coma and/or tail, without analyzing the generation mechanisms of this activity. The term refers to the fact that the activity is sporadic and is activated by some mechanism. So far, there is no consensus in the literature on whether there is a prevailing activation mechanism, and several alternatives have been discussed (see, e.g., Jewitt & Hsieh 2024).

To better understand the nature of these objects, we monitored 42 ACOs and 3 AAs in 2015 and 2026 using the telescope of the project Iniciativa de Mapeamento e Pesquisa de Asteroides nas Cercanias da Terra no Observatório Nacional (IMPACTON) of the Observatório Astronômico do Sertão de Itaparica (OASI). We detected activity in one of the observed ACOs (P/2015 PD$_{229}$), as well as the reactivation of two AAs (238P and 288P) (Martino et al. 2019). In 2019, the study of these objects was continued in order to expand the sample. To do this, we again worked with the IMPACTON telescope and with archive images from different databases and observatories. The objective of this work is to study the nature of the ACOs to determine whether they are dormant or extinct comets, or asteroids that escaped from the main belt and are currently in cometary orbits. To do this, we need to know the size of this population of objects and the number that are inactive or present at least low levels of activity. Meanwhile, studying AAs to determine activity and inactivity periods throughout their orbit can help us understand the activation mechanisms.

2. Observations

Images of ACOs and AAs were obtained from different instruments. Prior to this, we selected the set of ACOs to be studied based on the criterion developed by Tancredi (2014).

2.1. Selection of objects

We downloaded the asteroid database from the Minor Planet Center (MPC) and the comet database from the Jet Propulsion Laboratory (JPL) of NASA for updated orbital elements for the asteroids and comets. We only considered asteroids with precise orbital elements according to the uncertainty parameter U provided by the MPC. This parameter is an integer in the range from 0 to 9, where 0 indicates a very small uncertainty, and 9 extremely large uncertainty. Recently discovered objects usually have a very high U parameter that decreases as new observations are obtained and the orbits are improved. For our selection, we used a maximum of $U = 2$, which according to the MPC represents a longitude runoff error <19.6″ per decade. In this way, we ruled out asteroids whose orbital elements are considered of poor quality to avoid contaminating the sample with objects that might not in fact be ACOs. The uncertainty parameter tends to decrease over time, so that objects that were initially discarded because their uncertainty was too large may eventually fall within our criteria.

Next, Tancredi's criterion was applied. This separates the comets into JFC, Halley-type orbits (HTO), comets in asteroidal orbits (CAO), and Centaur comets (CC). HTOs have $T_{Jup} < 2$ and $a < a_{Nep}$; JFCs have $2 < T_{Jup} < 3.05$ and $q < Q_{Jup}$; CAOs have $T_{Jup} > 3.05$ and $q < Q_{Jup}$; and CCs have $T_{Jup} > 2$ and $Q_{Jup} < q < a_{Ura}$ (here, q is the object perihelion, Q_{Jup} is Jupiter aphelion, and a_{Ura} is Uranus semimajor axis). The ACOs are separated into ACOs-Jupiter family (ACOs-JF), ACOs-Centaur (ACOs-Cen), and ACOs-Halley orbits (ACOs-Hal). ACOs-JF have $2 < T_{Jup} < 3.05$ and $q < Q_{Jup}$, they are not in a resonance, and their values of the minimum orbital intersection distance (MOID) with respect to the giant planets are low; ACOs-Cen have $T_{Jup} > 2$ and $Q_{Jup} < q < a_{Ura}$; and ACOs-Hal have $T_{Jup} < 2$.

Finally, we numerically integrated the objects with the RADAU orbital element integrator (Everhart 1985) using orbital solutions from the MPC for asteroids and from JPL for comets (nominal orbits). The encounters of the objects with the giant planets were evaluated as well. When the ACO had no close encounters (less than 1 au) with any giant planet, it was removed from the list. After all these stages were completed, we generated tables with the data from selected ACOs[1].

---

[1] http://acos.astronomia.edu.uy

Table 1. Number of asteroids, ACOs, and comets.

Object	Quantity
Asteroids	1 103 617
Asteroids with precise orbits	955 049
Asteroids with $T_{Jup} < 3$	17 857
Asteroids with $T_{Jup} < 3$ and precise orbits	17 064
ACOs of the Jupiter family	384
ACOs in Halley orbit	115
ACOs Centaurs	206
Total	**705**
Jupiter family comets	603
Comets in Halley's orbit	110
Centaur comets	24
Comets in asteroidal orbits	31
Total	**768**

Table 1 shows the data of asteroids, asteroids with precise orbits, and asteroids with a Tisserand parameter with respect to Jupiter smaller than 3, with data taken in July 2021. The table also lists data of the objects that we obtained in the selection distinguished by type of ACO and type of comet. Although the number of asteroids with $T_{Jup} < 3$ is quite high, the number of ACOs is far lower when a strict dynamic criterion is applied. The sample of objects to be analyzed consists of all ACOs (705) and comets in asteroidal orbits (31). More than 17 000 asteroids with $T_{Jup} < 3$ were listed on the mentioned date, but only 705 of these meet the more stringent criteria established by Tancredi. These criteria ensure that the truly dynamical behavior of these objects is compatible with cometary dynamics.

2.2. Instruments

Images of ACOs and AAs were obtained from different instruments. An observation plan was designed in collaboration with the IMPACTON team of the OASI, Pernambuco, Brazil. The observatory is equipped with a 1m telescope. The images were taken with Apogee CCD cameras, model Alta U42 and Alta U47, with an R-Cousins filter. The details of the available instrumentation and sky characterization were reported by Rondón et al. (2020). Observations were made between August 2019 and April 2021. Most of the objects were observed only once, although some could be observed in two consecutive months. No restrictions on the true anomaly of the object were considered, although priority was given to observations close to perihelion. In most cases, two sequences of 15 images per object were taken. Bias, flat, and dark images were obtained to perform the basic calibration.

Through a collaboration with the Instituto de Astrofísica de Canarias (IAC) in Spain, we worked with a set of images of objects that were observed with the IAC80 telescope and the Jacobus Kapteyn Telescope (JKT) in 2015 and 2016. The IAC80 is located at the Teide Observatory on Tenerife, and the JKT is located at the Roque de los Muchachos Observatory on La Palma. Most of the observations with the IAC telescopes were made with the R filter, except for a few cases in which it was observed with the clear filter. Observations were made in November and December 2015, and between July and October 2016. The ACOs present in the images were selected with the same dynamic criteria as ours. The images provided to us

were processed on bias, dark, and flat, so no prior calibration was required.

In addition, we worked with archive images from the Very Large Telescope (VLT), a group of European telescopes belonging to the European Southern Observatory (ESO) at Cerro Paranal, Chile. These images were obtained with the Unit Telescopes (8.2 meters), with the instrument FOcal Reducer and low dispersion Spectrograph (FORS) (Appenzeller et al. 1998). We accessed the VLT images using two online tools: Mega Precovery (MP; Vaduvescu et al. 2013) and Solar System Object Image Search (SSOIS; Gwyn et al. 2012). We obtained images in the filters *V*, *R*, and *I*. The images corresponded to different projects that observed these objects of interest, including Romon-Martin et al. (2002), Doressoundiram et al. (2005), Lorin & Rousselot (2007), DeMeo et al. (2008), Belskaya et al. (2010), and Tozzi et al. (2012). For most of the objects, no associated publications were found.

Finally, we used images from the Dark Energy Survey (DES), which is an international collaborative project that observed the sky over six years since 2013 and covered an area of 5000 square degrees of the celestial southern hemisphere. Observations were made in filters grizY. The instrument that was used is an extremely sensitive 570-megapixel digital camera, the Dark Energy Camera (DECam; see Flaugher et al. 2015), and it is located on the 4-meter Blanco telescope of the Cerro Tololo Inter-American Observatory. A total of 3374 images containing the coordinates of 195 different objects were obtained. In this archival search, the selection was not based on the predicted apparent magnitude of the objects. This led to cases in which the objects that were nominally within the instrument field of view were too faint to be recovered in the images. There were also no restrictions regarding the true anomaly of objects.

3. Data reduction

Two methods were used to detect activity on the objects: an analysis of the surface brightness profiles, and deviations in the reduced magnitude along the orbit.

3.1. Surface brightness profiles

Following the method described by Luu (1992), we applied the approach used previously by Martino et al. (2019). This technique involves comparing the surface brightness profiles of asteroids with those of stars. A widened profile indicates the existence of a cometary coma, and a profile similar to the stellar one corresponds to an object without activity.

All images were processed trough Python and Matlab scripts. The usual calibration was performed, along with the removal of bad pixels and cosmic rays. A plate solution was performed using Astrometry.net routines[2]. If there were image sequences, these were aligned on the stars and on the object, and the aligned images were added to increase the signal-to-noise ratio (S/N). The position of the object in the image was automatically calculated using JPL ephemerides.

The radial surface brightness profile of the object was obtained by fitting a Moffat function to the flux values as a function of the distance to the centroid. The same procedure was employed with a set of stars, and we obtained an average profile. Both profiles were plotted superimposed, and a visual inspection was performed with each plot in search of deviations.

---

[2] https://astrometry.net

Some of the archival images we obtained had long exposure times (more than 90 seconds), and in some cases, this caused an object to appear in the image as a trail. It was therefore not possible to obtain a radial profile. For these cases, we obtained the displacement values in right ascension and declination, and we rotated the image so that the trail remained horizontal in the image (this technique is more similar to the original proposed by Luu 1992). The average of the flux by rows was calculated, and then, we obtained the value of the centroid to plot the profiles.

3.2. Reduced magnitudes

The reduced magnitude is the magnitude that an object would have at a heliocentric distance $r = 1$ au, a geocentric distance $\Delta = 1\,au$, and a phase angle $\alpha = 0^o$ (the absolute magnitude for a Solar System object is obtained from averaging several measurements of its reduced magnitude). For an inactive object (a bare nucleus), the reduced magnitude is expected to vary according to the rotational light curve. The rotation of the object generates a maximum amplitude in magnitude (A_{max}) according to Eq. (2), where a and b are the axes of the object. For example, a 1:5 axis ratio would generate a maximum amplitude of 1.75 magnitudes,

$$A_{max} = 2.5 \log \frac{a}{b}. \tag{2}$$

The study of the reduced magnitude versus the heliocentric distance enables us to find changes in brightness along the orbit of the objects, which serve as indicators of cometary activity. When an object is active, its brightness increases and its reduced magnitude decreases. It is therefore useful to detect these changes in brightness to generate plots of the reduced magnitude as a function of heliocentric distance with the available photometric data.

We used magnitude reports from different observers that are available in the MPC database. The limitations of this dataset were discussed in Martino et al. (2019), but the conclusion was that these observations provide a feasible approach to monitoring the object at various points in its orbit. This cannot be achieved by a single observer. Additionally, magnitudes computed from the data obtained from the different telescopes were added to the data. The apparent magnitudes were reduced by geocentric and heliocentric distance, as well as by phase angle, with a phase coefficient $\beta = 0.04$ mag/deg, according to Jewitt & Luu (1989) (Eqs. (3) and (4)) and were also transformed to a common band V by applying color corrections of a solar-like spectrum,

$$m(1, 1, \alpha) = m(r, \Delta, \alpha) - 5\log(r\Delta) \tag{3}$$

$$m(1, 1, 0) = m(1, 1, \alpha) - \beta\alpha. \tag{4}$$

The values of the reduced magnitude were plotted as a function of the heliocentric distance. All MPC data were used when their ephemerides matched those of the object at the time of observation. Data belonging to large surveys were highlighted in the plot. Then, we searched for significant differences between the calculated magnitudes and the reported average that could not be explained by other factors. We specifically searched for cases with more than one report of brightening, corresponding to different nights of observation and/or observers.

4. Results

The results of the profiles are presented in Sect. 4.1, and those of the reduced magnitudes are described in Sect. 4.2.

Table 2. Summary of the profiles.

Quality	ACOs	Profiles	AAs	Profiles
High	53	158	1	4
Medium	38	90	4	7
Low	34	126	2	4
Trails	8	24	0	0
Total	133	398	7	15

Table 3. Summary of the objects by instrument.

Object	OASI	IAC	VLT	DES	Total[(*)]
ACOs	33	5	20	88	133
AAs	2	0	4	4	7
Total	35	5	24	92	140

Notes. [(*)]Objects that were observed by more than one instrument were considered only once.

4.1. Surface brightness profiles

A total of 413 surface brightness profiles of 140 studied objects were obtained because many of the objects were observed on different dates, and we therefore obtained several profiles per object. Table 2 shows the number of ACOs and AAs with a well-defined surface brightness profile, and their quality. The quality depends on the observation conditions and S/N of the object. The following values were adopted to define it, following Martino et al. (2019): A profile was considered to be of high quality when the mean deviation of the flux values did not exceed 5% of the normalized flux. A medium quality ranged between 5 and 10%, and a low quality meant that it exceeded 10%. To calculate the mean deviation, we selected a range of pixels (measured from the centroid of the object), typically between 4 and 8. These values were adjusted according to the night seeing. An object was considered to have high quality when at least one profile had this quality. The quality was considered to be medium when the best profile had this quality, and the quality was considered to be low when the profiles only had this quality. When the object appeared as a trail in the image, no quality calculations were made because only a few intensity values were available to make an adjustment. These objects appear in Table 2 as "Trails". Although the data quality differs mainly depending on the brightness of the object, inactive objects are expected to present a similar profile to that of stars, regardless of the data dispersion.

Table 3 shows the number of ACOs and AAs with at least one profile, sorted by instrument (the totals consider objects without repetitions). The details of each observation can be found in Appendix A.

All brightness profiles were inspected for deviations from a stellar profile. For objects 29981, 54598, 90572, 515718, and 2015 BK$_{22}$, at least one deviating profile was obtained. This might be an indication of slight cometary activity (Figs. 1a, b, c, d, and e, respectively). For C/2014 OG$_{392}$ (PANSTARRS), we obtained a profile with a considerable widening, but with a high dispersion (Fig. 1f). This object has already been classified as a comet. The activity was discovered in archival images from July and August 2017, and it was confirmed with observations from August 2019 (Chandler et al. 2020). Our data corresponded to November 2018, which is between the two existing activity
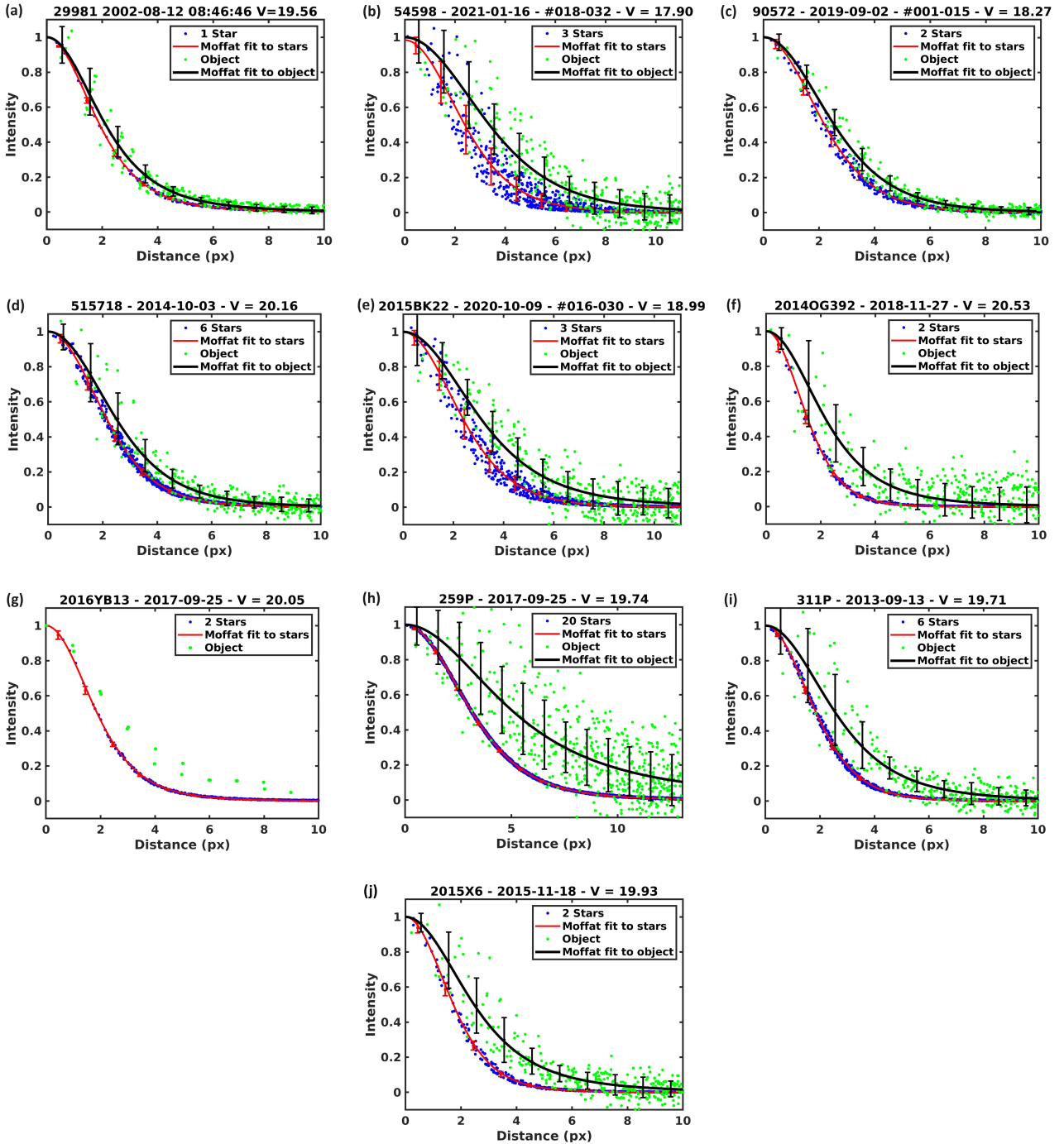
Fig. 1. Surface brightness profiles of (a) 29981 (VLT), (b) 54598 (IMPACTON), (c) 90572 (IMPACTON), (d) 515718 (DES), (e) 2015 BK$_{22}$ (IMPACTON), (f) 2014 OG$_{392}$ (DES), (g) 2016 YB$_{13}$ (DES), (h) 259P (DES), (i) 311P (DES), and (j) P/2015 X$_6$ (DES). The plots show the normalized intensity values of each pixel from the centroid for one or more stars (blue dots), the Moffat fit of the stars (red line), the normalized intensity values of the object (green dots), and the Moffat fit of the object (black line). The red error bars correspond to the stars and the black error bars to the object. The errors were calculated from the dispersion of the flux values with respect to the fit. A small artificial horizontal offset has been introduced in the position of the bars to avoid overlap. In the image header we list the object name, date, image range (when a set of images was coadded), image number or time, and the calculated magnitude. When the object appeared as a trail (2016 YB$_{13}$), the intensity values of the trail are plotted superimposed with the profile of the stars (with their Moffat fit).

reports, and they were obtained from the DES project. Object 2016 YB$_{13}$ appeared in the DES images as a trail. We obtained the profile shown in Fig. 1g, where the intensity values of the object appear to be clearly separated from the star profile.

Widened profiles were also obtained for three AAs: 259P, 311P, and P/2015 X$_6$ (Figs. 1h, i, and j). In all cases, the activity

was verified. For 259P and 311P, this is consistent with existing reports. In the first case, activity was present in DES images from September 2017, when it reactivated (Hsieh et al. 2017). Object 311P was also in DES images from September 2013. In this month, the first reports of activity (Bolin et al. 2013) were obtained. P/2015 X$_6$ showed a widened profile in DES images

from November 18, 2015, and the first activity for this object was reported on December 7, 2015 (Tubbiolo et al. 2015). Finally, 133P was present in images from July 2007 during its second activity episode. However, the profiles were not visibly widened. This outcome agrees with the findings of Hsieh et al. (2010), who studied the reactivation of the object. Their analysis revealed that while the object exhibited activity, the full width at half maximum (FWHM) of its brightness profile matched that of a stellar FWHM during those observations. This suggests that the object either lacked a coma or had an extremely compact one (smaller than $1''$, corresponding to a linear diameter of 1200 km).

4.2. Reduced magnitude

We created plots of the reduced magnitude as a function of the heliocentric distance for the 705 ACOs in the list and for the 7 AAs observed during this work, in which we included all the data from photometric observations reported to the MPC. The magnitudes calculated from the images we analyzed were also added to the data. The reduced magnitude plots of all the ACOs in our list were reviewed, and those with more than one report with brightening in the MPC data were separated. A summary analysis of these cases is presented below.

Objects 322966, 323137, and 2009 KF_{37} (Figs. 2c) differed from the absolute magnitude H. We were unable to attribute this to object rotation. The reports for 322966 correspond to a single observer and there are no other reports for the same dates, while two reports were made for 2009 KF_{37} from different observatories in different years. Object 323137 has already been classified as a comet (282P). This object belongs to the outer belt, and its Tisserand parameter is $T_J = 2.99$. It was observed to be active in 2013 and was found to also have activity in images taken in March 2012 (Bolin et al. 2013). The plots of the reduced magnitude show three brightening peaks with respect to the average magnitude, which correspond to reports made in 2001 (first observations of the object), 2003, and 2004. In particular, in July 2004, observers reported magnitudes between 12.54 and 13.14, and the absolute magnitude of the object is $H = 15.3$. Objects 275618 and 2017 QO_{33} (Figs. 2d and e) were present in several MPC reports in which a magnitude with an increased brightness was obtained. The reports corresponded to a single observatory, however, and other observers reported magnitudes close to the mean for the same dates.

On the other hand, we reviewed the plots in which the observations made during this work were included (our data appear in the plots as red squares). Three cases differ from the absolute magnitude of the MPC, considering the error in calculated magnitude: 54598, 2000 CN_{152}, and 2014 SS_{303} (Figs. 2f, g, and h). Only object 54598 also showed a widened profile. The case of 2000 CN_{152} was discarded because the object was at the edge of the image, which may have caused a distortion in the flux values.

5. Discussion

We first discuss the results for the ACOs. Based on the criteria employed in this study, there are a total of 705 of these objects. We obtained surface brightness profiles of 133 ACOs and generated a cumulative total of 160 (considering our previous work). A total of 92 of these were identified as ACOs-JF, 50 as ACOs-Cen, and 18 as ACOs-Hal. Figure 3 shows the histograms of the heliocentric distance (r) of the objects at the time of observation. The data are categorized based on the heliocentric distances, specifically distinguishing between those at a distance smaller than and larger than 5 au.

We employed two activity indicators: (i) deviations in the brightness profile relative to the stellar profile, and (ii) a significant decrease in the reduced magnitude of the object.

The deviations of 7 of the 133 ACOs for which profiles were obtained cannot be attributed to external factors such as observability conditions or low S/N. These ACOs are 29981, 54598, 90572, 515718, C/2014 OG_{392} (PANSTARRS), 2015 BK_{22}, and 2016 YB_{13}. One of these asteroids has already been classified as a comet. Moreover, a similar case of activity was previously documented for one of the objects we investigated in our prior study, that is, for the object that was originally classified as an asteroid and then as comet P/2015 PD_{229} ISON-Cameron (Martino et al. 2019). We found possible signs of activity for 8 of the 160 ACOs based on the surface profiles (5%).

By examining the reduced magnitude, we identified five objects with noteworthy deviations: 54598, 322966, 323137, 2009 KF37, and 2014 SS303. One of these objects is also officially classified as a comet: 282P (323137). In our previous study, only one ACO varied significantly in its reduced magnitude: 174P/(60558) Echeclus, which was also already classified as an asteroid and a comet. We found possible activity based on the reduced magnitudes for 6 of the 705 ACOs (<1%).

Figure 4 shows the histograms of the true anomalies (f) for our objects. We compare those with and those without signs of activity. Objects with signs of activity tend to cluster around perihelion, and their f values range from $-50°$ to $50°$. However, it is crucial to acknowledge that the peak in the distribution of f for all observed objects also falls within the same range $[-50°, 50°]$. We cannot rule out that the proximity to perihelion of active objects may be influenced by a potential selection bias. We attribute the concentration near perihelion in the distribution of the observed objects to their increased brightness during this period, which leads to a prioritized selection based on observational considerations.

Two hypotheses are currently considered regarding the origin of the ACO population: (i) they are fully inert comets; or (ii) they are asteroids that escaped from the main belt. Our findings reveal a notably low percentage of active objects or objects with signs of activity, which would rule out a smooth continuum from active to inert comets. Consequently, the transition from an active to a fully inactive state appears to be abrupt. Alternatively, a significant majority of these objects may indeed be escaped asteroids. In light of this, further analysis of the dynamic routes from the main belt to the ACOs is warranted.

One population that might contribute to the group of objects that has dynamical similarities with JFCs and yet remain inactive are the Hilda asteroids. Previous studies, such as those by Di Sisto et al. (2003) and Di Sisto et al. (2005), have suggested that Hildas might be a plausible source of JFCs, which would supplement the primary sources of the trans-Neptunian region and Jupiter trojans. Hildas that successfully escape resonance are dynamically controlled by Jupiter, and their behavior is similar to that of JFCs. Notably, a subset of comets known as quasi-Hilda type (Kresak 1979; Tancredi et al. 1990) shares orbital characteristics with Hilda asteroids (large q, low-eccentricity orbits near the 3:2 resonance with Jupiter), but this subset remains unstable. This underscores the potential role of Hilda asteroids in contributing to the population of objects with JFC-like dynamics. Additionally, as highlighted by Di Sisto et al. (2019), certain trojans that escape their stability zones might contribute to the population of ACOs. These contributions are lower than those to other populations, however.

The population of NEAs is another potential contributor. Fernández et al. (2014) analyzed the dynamic behavior of a
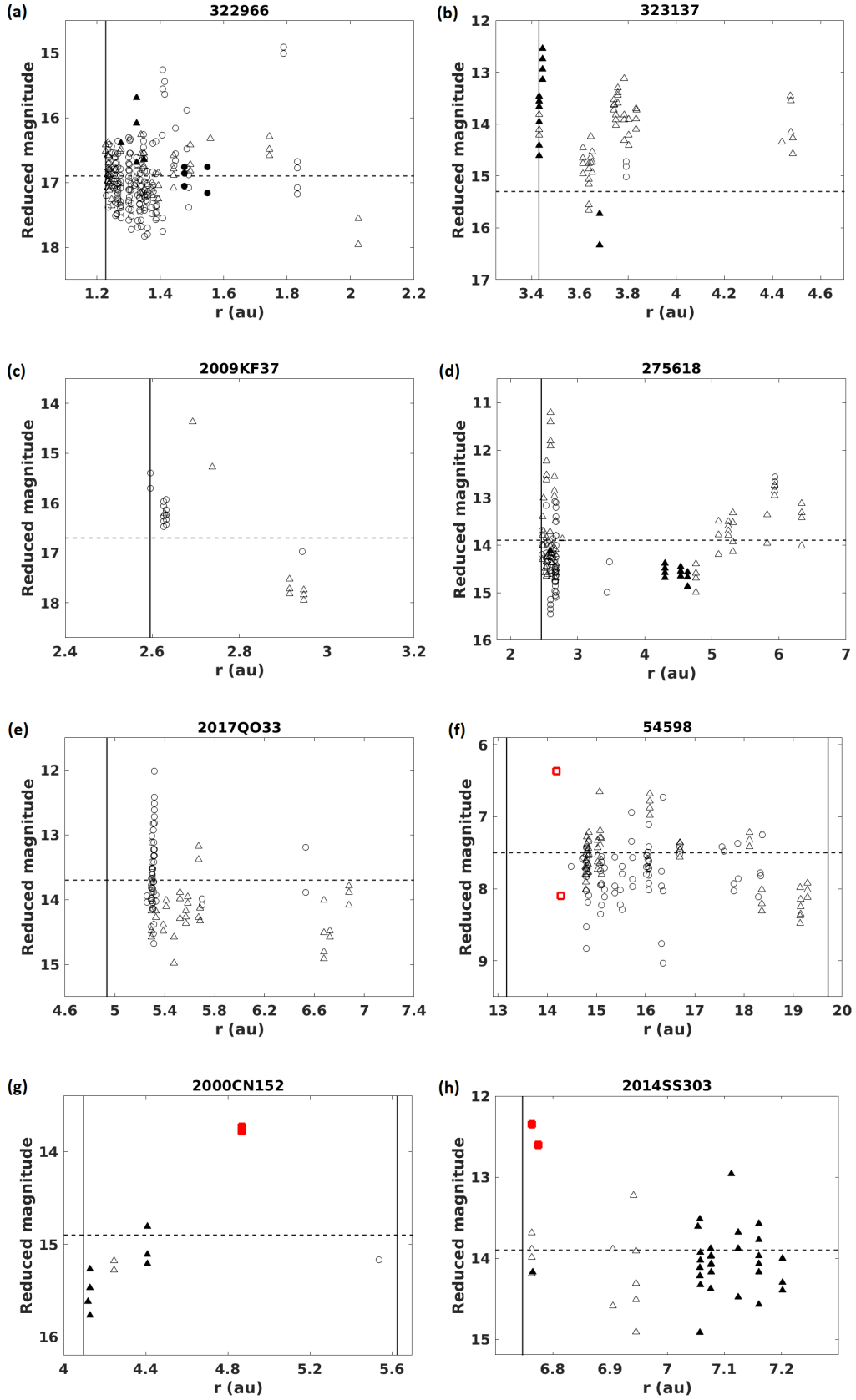
Fig. 2. Reduced magnitude of (a) 322966, (b) 323173, (c) 2009 KF$_{37}$, (d) 275618, (e) 2017 QO$_{33}$, (f) 54598, (g) 2000 CN$_{152}$, and (h) 2014 SS$_{303}$. The vertical line on the left indicates the perihelion distance of the object. In some cases, a vertical line is also plotted to the right, indicating the aphelion distance. The dotted horizontal line shows the MPC catalog absolute magnitude, which it is taken as a reference. The empty symbols correspond to observations made before passing through perihelion ($f > 180°$), and filled symbols correspond to observations after perihelion passage ($f < 180°$). The data plotted with triangles correspond to large surveys, black circles correspond to any other MPC data, and red squares show the data obtained in this work. The scales are different for each image because they are adjusted to the data values of each object.
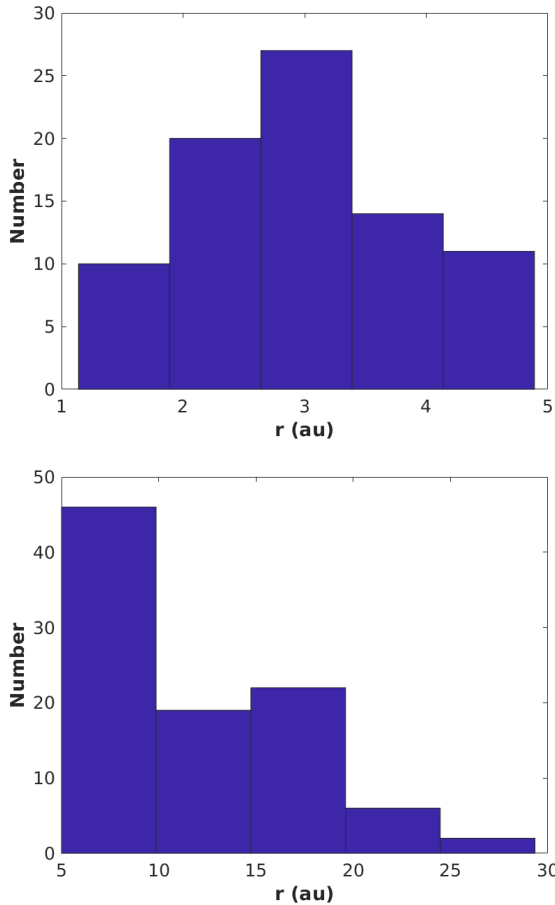
Fig. 3. Histogram of the heliocentric distances of the observed ACOs between 0 and 5 au (top) and at more than 5 au (bottom).
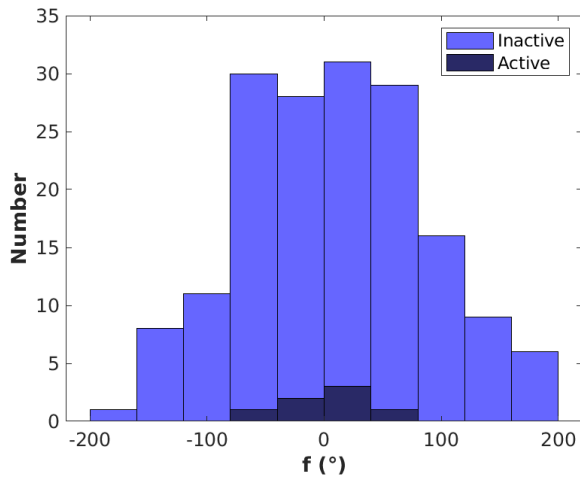

Fig. 4. Histogram of the true anomalies of observed ACOs with and without activity.

subset of NEAs that closely approach or even cross the orbit of Jupiter. While the majority of these NEAs follow typical asteroidal orbits, a distinct subset displays highly unstable orbits similar to those of JFCs. The authors suggested that these specific NEAs might be inactive comets. The hypothesis that NEAs are potentially inactive comets is supported by various studies, both observationally and through modeling of their physical

evolution. For instance, Fernández et al. (2005) and DeMeo & Binzel (2008) estimated that a percentage (4–8%) of NEOs exhibit physical and dynamical properties that are indicative of a cometary origin from the outer Solar System. Additionally, recent studies by Seligman et al. (2023) suggested the existence of a distinct dark comet population that consists of NEOs that show non-gravitational accelerations without visible cometary activity. This further supports the hypothesis of a cometary origin for certain NEAs.

The physical studies of the spectra and albedos conducted by various researchers support the hypothesis of the cometary nature of ACOs. Works such as those by Licandro et al. (2008), Kim et al. (2014), Licandro et al. (2016), and Licandro et al. (2018) consistently showed that many ACOs exhibit physical characteristics that are compatible with those of cometary nuclei. For the spectra, these studies showed that the majority of observed ACOs are of type D or P, which is also compatible with them coming from the Hilda or Trojan populations (DeMeo & Carry 2014).

Regarding physical modeling, Rickman et al. (1990) conducted simulations to explore the formation of stable dust mantles in short-period comets. These mantles are characterized by typical sizes of centimeters and can show small cracks resulting from collisions. These cracks can lead to the exposure of active regions, which maintain the comet in a state of low activity. Furthermore, the model suggests that enduring crusts might form, in particular, in objects with perihelic distances exceeding 2 au and featuring nuclei with diameters of several kilometers.

Although observational studies suggested that a substantial percentage of ACOs might be cometary nuclei, very few cases of activity were in fact detected. At least a residual of activity would be expected from this population. Díaz & Gil-Hutton (2008) analyzed the potential activation of ACOs due to impacts, particularly if they harbor subsurface volatiles. The authors discovered an excess in the number of candidates for dormant comets beyond what was expected. This finding implies that the ACO population might encompass objects that are not comets in a dormant state.

The criterion we used yields a total of 31 AAs. We studied 7 of them, 4 of which were active in the images. Figure 5 shows the projected orbit on to the ecliptic for each object as seen from the north ecliptic pole. The perihelion location is indicated, as are the places where activity was observed. The observations we analyzed are included.

Objects 324P, 331P, and 354P were not active in our observations. The first object was observed a month prior to its reactivation. Our observations of 331P and 354P did not coincide with a reactivation event.

Table 4 summarizes our observations and indicates whether they coincided in time and space with known activity episodes. In several instances, our observations aligned with the same orbital regions in which activity was observed previously. For objects with widened profiles, our data corresponded to periods in which they had already been noted as active. A noteworthy example is P/2015 X_6, where our DES images captured earlier instances than the first available reports. This extends the known active period.

Our observations revealed that episodes of activity are highly constrained in time and do not consistently reoccur in the same orbital region. This observation raises questions about the assumption of an assured recurrence of activity episodes, and it challenges the existing sublimation hypothesis for some of these objects.
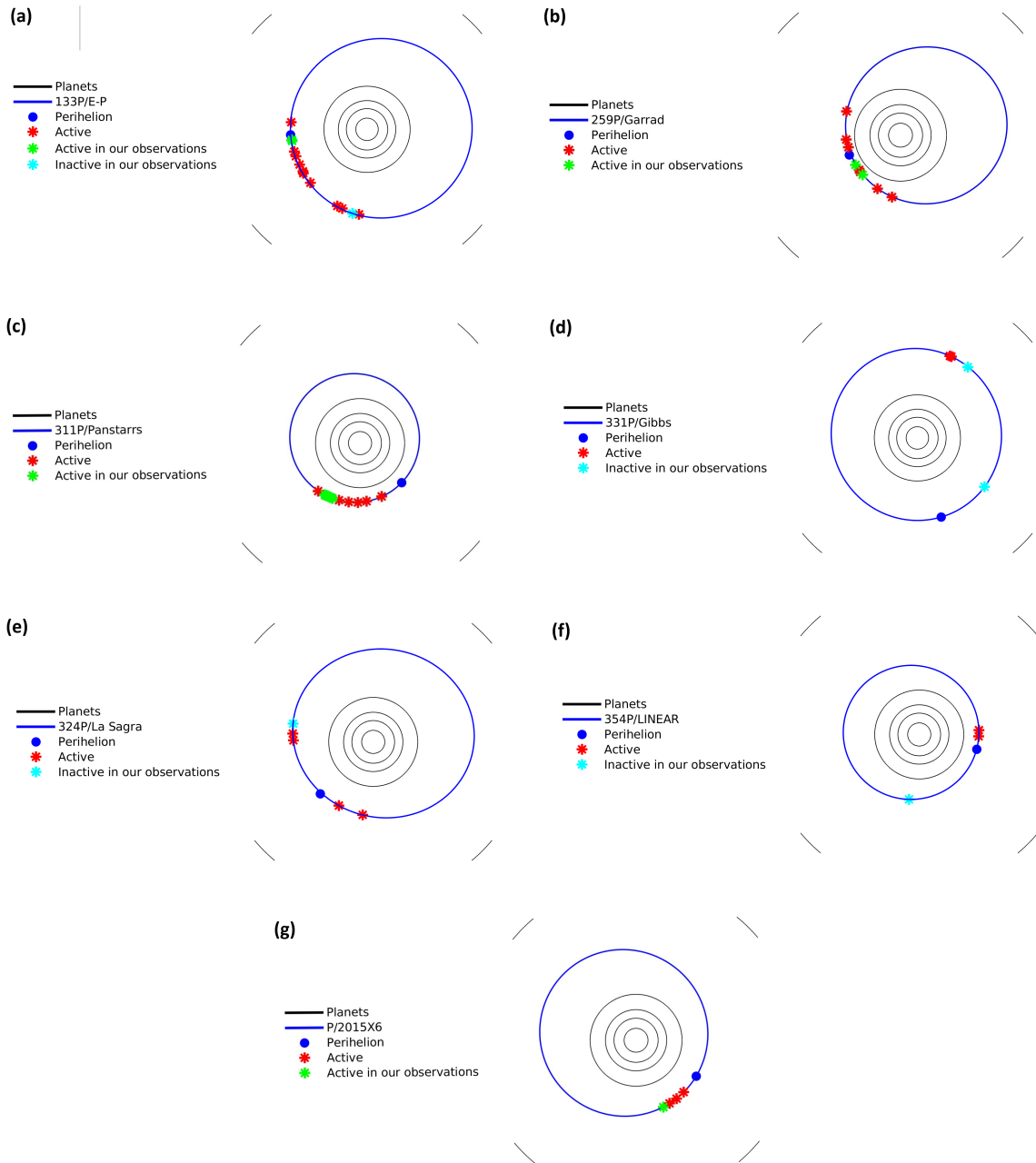
Fig. 5. Orbits of (a) 133P, (b) 259P, (c) 311P, (d) 331P, (e) 324P, (f) 354P, and (g) P2015 X_6. The black lines represent the orbits of the planets, the blue line shows the orbit of the object, the blue circle shows its perihelion, the red asterisks show the places where activity has been observed, the green asterisks represent the observations made during this work in which activity was confirmed, and the cyan asterisks indicate were no activity was found. The view is from the north ecliptic pole, so that the movement of the objects in their orbits is counterclockwise.

6. Conclusions and future work

The objective of this work was to monitor the possible activity of ACOs and AAs. We started from a dataset that was analyzed in 2015 and 2016 and extended the list of studied objects to achieve a significant sample. We worked with images obtained from different databases, as well as with new observations made between 2019 and 2021.

We increased the ACO sample of analyzed objects from 7% to 23% compared to the previous work. Our results indicate that a majority fraction within the ACOs-JF population (~400) might be escaped asteroids, with a few cases of dormant comets.

The AA sample was increased to 32% of the known objects. Of the 7 objects we studied, 4 were active in the images. Some objects were active in regions in which activity was observed before, while others were inactive in the same regions or close to them.

Although the sample of objects we studied was considerably extended and allowed us to gain a more complete picture of transitional objects, we understand that there are currently several open questions that could be addressed as future work. For a more conclusive understanding of the nature of ACOs, a comprehensive analysis is imperative. This should encompass an in-depth analysis of the dynamic pathways leading from the

Table 4. Activated asteroid observations.

Object	Date	Observations
133P	07/2007	Active in the same region during active passage.
	08/2019	Inactive in region where it was active.
259P	09/2017	Active in the same region during active passage.
311P	09/2013	Active in the same region during active passage.
324P	04/2015	Inactive in the same region one month before active passage.
331P	12/2015	Inactive in region without activity.
	03/2017	Inactive near the region where it was active in 2012.
354P	04/2015	Inactive in region without activity.
P/2015 X_6	11/2015	Active in the same region 3 weeks before active passage.

main asteroid belt to the chaotic dynamics observed in ACOs. Additionally, a thorough investigation of the relative contributions from different populations and a spectroscopic comparison between ACOs-JF and their source populations are essential components of this analysis.

Furthermore, an exploration of the various mechanisms that cause the activation of asteroids is also necessary. Through such an analysis, we can move closer to a definitive conclusion about the nature of activity in these bodies.

Finally, first results from the recent NASA-DART mission to the Dydimos-Dimorphos binary system show that an artificially activated asteroid was generated (Li et al. 2023), as proposed by Tancredi et al. (2023). The duration of the increase in brightness with respect to the pre-impact magnitude and the evolution of the dust tail helps us better understand the activation process of an asteroid (Li et al. 2023).

References

Alvarez-Candal, A. 2013, A&A, 549, 10
Alvarez-Candal, A., & Roig, F. 2005, IAU Colloq., 197, 205
Appenzeller, I., Fricke, K., Fürtig, W., et al. 1998, The Messenger, 94, 1
Belskaya, I. N., Bagnulo, S., Barucci, M. A., et al. 2010, Icarus, 210, 472
Bolin, B., Denneau, L., Veres, P., et al. 2013, Centr. Bur. Elec. Tel., 3559, 1
Chandler, C. O., Kueny, J. K., Trujillo, C. A., Trilling, D. E., & Oldroyd, W. J. 2020, ApJ, 892, L38
Chandler, C. O., Trujillo, C. A., Oldroyd, W. J., et al. 2024, AJ, 167, 156
DeMeo, F., & Binzel, R. P. 2008, Icarus, 194, 436
DeMeo, F. E., & Carry, B. 2014, Nature, 505, 629
DeMeo, Fornasier, S., Barucci, M. A., et al. 2008, AAS/Div. Planet. Sci. Meeting Abs., 40, 47.05
Díaz, C. G., & Gil-Hutton, R. 2008, A&A, 487, 363
Di Sisto, R. P., Brunini, A., Dirani, L. D., & Orellana, R. B. 2003, Boletin de la Asociacion Argentina de Astronomia La Plata Argentina, 46, 11
Di Sisto, R. P., Brunini, A., Dirani, L. D., & Orellana, R. B. 2005, Icarus, 174, 81
Di Sisto, R. P., Fernández, J. A., & Brunini, A. 2009, Icarus, 203, 140
Di Sisto, R. P., Ramos, X. S., & Gallardo, T. 2019, Icarus, 319, 828
Doressoundiram, A., Barucci, M. A., Tozzi, G. P., et al. 2005, Planet. Space Sci., 53, 1501
Elst, E. W., Pizarro, O., Pollas, C., et al. 1996, IAU Circ., 6456, 1
Everhart, E. 1985, Astrophys. Space Sci. Lib., 115, 185
Fernández, Y. R., Jewitt, D. C., & Sheppard, S. S. 2005, AJ, 130, 308
Fernández, J. A., Sosa, A., Gallardo, T., & Gutiérrez, J. N. 2014, Icarus, 238, 1
Flaugher, B., Diehl, H. T., Honscheid, K., et al. 2015, AJ, 150, 150
Geem, J., Ishiguro, M., Bach, Y. P., et al. 2022, A&A, 658, A158
Gwyn, S. D. J., Hill, N., & Kavelaars, J. J. 2012, PASP, 124, 579
Hsieh, H. H. 2017, Phil. Trans. R. Soc. London Ser. A, 375, 2097
Hsieh, H. H., & Haghighipour, N. 2016, Icarus, 277, 19
Hsieh, H., & Jewitt, D. 2006, Science, 312, 561
Hsieh, H. H., Jewitt, D. C., & Fernández, Y. R. 2004, AJ, 127, 2997
Hsieh, H. H., Jewitt, D., Lacerda, P., Lowry, S. C., & Snodgrass, C. 2010, MNRAS, 403, 363
Hsieh, H. H., Ishiguro, M., Kim, Y., et al. 2017, AAS/Div. Planet. Sci. Meeting Abs., 49, 305.10
Jewitt, D., & Hsieh, H. H. 2024, in Comets III, eds. K. J. Meech, M. R. Combi, D. Bockelée-Morvan, S. N. Raymodn, & M. E. Zolensky (Tucson: University of Arizona Press), 767
Jewitt, D., & Luu, J. 1989, AJ, 97, 1766
Kim, Y., Ishiguro, M., & Usui, F. 2014, ApJ, 789, 151
Kresak, L. 1979, Dynamical Interrelations Among Comets and Asteroids., eds. T. Gehrels, & M. S. Matthews (Tucson:, University of Arizona Press), 289
Li, J., Hirabayashi, M., Farnham, T., et al. 2023, Nature, 616, 452
Licandro, J., Alvarez-Candal, A., de León, J., et al. 2008, A&A, 481, 861
Licandro, J., Alí-Lagoa, V., Tancredi, G., & Fernández, Y. 2016, A&A, 585, A9

Licandro, J., Popescu, M., de León, J., et al. 2018, A&A, 618, A170
Lorin, O., & Rousselot, P. 2007, MNRAS, 376, 881
Luu, J. X. 1992, Icarus, 97, 276
Martino, S., Tancredi, G., Monteiro, F., Lazzaro, D., & Rodrigues, T. 2019, Planet. Space Sci., 166, 135
Rickman, H., Fernández, J. A., & Gustafson, B. A. S. 1990, A&A, 237, 524
Romon-Martin, J., Barucci, M. A., de Bergh, C., et al. 2002, Icarus, 160, 59
Rondón, E., Lazzaro, D., Rodrigues, T., et al. 2020, PASP, 132, 065001
Seligman, D. Z., Farnocchia, D., Micheli, M., et al. 2023, PSJ, 4, 35
Simion, G., Popescu, M., Licandro, J., Vaduvescu, O., & de León, J. 2020, European Planetary Science Congress, 351
Tancredi, G. 2014, Icarus, 234, 66
Tancredi, G., Lindgren, M., & Rickman, H. 1990, A&A, 239, 375
Tancredi, G., Liu, P.-Y., Campo-Bagatin, A., Moreno, F., & Domínguez, B. 2023, MNRAS, 522, 2403
Tozzi, G.-P., Bagnulo, S., Barucci, M. A., et al. 2012, AAS/Div. Planet. Sci. Meeting Abstracts, 44, 310.15
Tubbiolo, A. F., Bressi, T. H., Wainscoat, R. J., et al. 2015, Minor Planet Electronic Circulars, 2015-X180
Vaduvescu, O., Popescu, M., Comsa, I., et al. 2013, Astron. Nachr., 334, 718
Ye, Q.-Z., Brown, P. G., & Pokorný, P. 2016, MNRAS, 462, 3511

[1] Departamento de Astronomía, Facultad de Ciencias, Universidad de la República, Iguá 4225, 11400 Montevideo, Uruguay
[2] Observatório Nacional, R. Gen. José Cristino 77 - São Cristóvão, Rio de Janeiro, RJ - 20921-400, Brazil
[3] Laboratório Interinstitucional de e-Astronomia - LIneA, Av. Pastor Martin Luther King Jr, 126, Rio de Janeiro - RJ - 20765-000, Brazil
[4] Instituto de Astrofísica de Canarias, C/ Vía Láctea s/n, 38205 La Laguna, Tenerife, Spain
[5] Department of Physics, University of Michigan, Ann Arbor, MI48109, USA
[6] Astronomy Department, University of Washington, Box 351580, Seattle, WA 98195, USA
[7] Department of Physics & Astronomy, University College London, Gower Street, London, WC1E 6BT, UK
[8] Institut de Física d'Altes Energies (IFAE), The Barcelona Institute of Science and Technology, Campus UAB, 08193 Bellaterra (Barcelona) Spain
[9] School of Mathematics and Physics, University of Queensland, Brisbane, QLD 4072, Australia
[10] Centro de Investigaciones Energéticas, Medioambientales y Tecnológicas, Madrid, Spain
[11] Fermi National Accelerator Laboratory, PO Box 500, Batavia, IL 60510, USA
[12] California Institute of Technology, 1200 East California Blvd, MC 249-17, Pasadena, CA 91125, USA
[13] Instituto de Fisica Teorica UAM/CSIC, Universidad Autonoma de Madrid, 28049 Madrid, Spain
[14] Institut d'Estudis Espacials de Catalunya (IEEC), 08034 Barcelona, Spain
[15] Institute of Cosmology and Gravitation, University of Portsmouth, PO1 3FX, UK
[16] University Observatory, Faculty of Physics, Ludwig-Maximilians-Universität, Scheinerstr. 1, 81679 Munich, Germany
[17] Center for Astrophysical Surveys, National Center for Supercomputing Applications, Urbana, IL 61801, USA
[18] Santa Cruz Institute for Particle Physics, Santa Cruz, CA 95064, USA
[19] Center for Astrophysics | Harvard & Smithsonian, Cambridge, MA 02138, USA
[20] Australian Astronomical Optics, Macquarie University, North Ryde, NSW 2113, Australia
[21] Department of Physics and Astronomy, Texas A&M University, College Station, TX 77843, USA
[22] LPSC Grenoble - 53, Avenue des Martyrs 38026 Grenoble, France
[23] Kavli Institute for Particle Astrophysics & Cosmology, Stanford University, Stanford, CA 94305, USA
[24] SLAC National Accelerator Laboratory, Menlo Park, CA 94025, USA
[25] Department of Physics, Northeastern University, Boston, MA 02115, USA
[26] Physics Department, Lancaster University, Lancaster, LA1 4YB, UK
[27] Computer Science and Mathematics Division, Oak Ridge National Laboratory, Oak Ridge, TN 37831, USA
[28] Department of Physics, University of Michigan, Ann Arbor, MI 48109, USA
[29] Department of Astronomy, University of California, Berkeley, CA 94720, USA
[30] Lawrence Berkeley National Laboratory, 1 Cyclotron Road, Berkeley, CA 94720, USA

Appendix A: Observational data of studied objects

Observational information regarding ACOs is presented in Table A.1, while that related to AAs can be found in Table A.2. Tables contain date of observation, geocentric distance (Δ), heliocentric distance (r), true anomaly (f), and observatory used.

Table A.1. Observational information for ACOs.

Object	Date	Δ (au)	r (au)	f (deg)	Observatory[1]
944	2016 Sep 13	5.45	5.96	226.2	DES
	2017 Sep 30	3.20	3.92	254.6	DES
2060	2013 Sep 11	16.62	17.62	152.5	DES
	2014 Oct 21	17.22	17.95	156.8	DES
	2015 Sep 29	17.24	18.19	160.3	DES
	2015 Oct 18	17.40	18.21	160.5	DES
	2015 Nov 01	17.57	18.21	160.6	DES
	2016 Sep 26	17.43	18.41	163.8	DES
	2016 Oct 05	17.47	18.41	163.9	DES
	2016 Nov 05	17.80	18.43	164.2	DES
	2017 Oct 26	17.80	18.60	167.6	DES
	2017 Nov 09	17.98	18.60	167.7	DES
	2019 Sep 28	17.81	18.81	174.2	OASI
5164	2019 Nov 23	1.23	2.22	300.8	OASI
6144	2016 Jul 05	3.27	4.19	92.2	IAC
	2018 Sep 09	5.14	6.08	152.0	DES
	2018 Oct 19	5.20	6.13	154.1	DES
	2018 Nov 09	5.42	6.16	155.3	DES
	2019 Sep 28	5.52	6.44	171.4	OASI
	2019 Nov 30	5.74	6.47	174.4	OASI
8405	2001 Jun 13	6.20	7.16	332.0	VLT
10199	2008 Feb 04	13.30	13.40	32.5	VLT
20898	2020 Aug 21	3.65	4.40	121.5	OASI
29981	2000 Sep 05	11.46	12.38	9.6	VLT
	2002 Aug 12	12.80	13.14	30.3	VLT
30512	2016 Jul 05	2.48	3.14	73.2	IAC
44594	2013 Sep 08	19.34	20.34	304.4	DES
	2014 Oct 14	18.97	19.85	309.2	DES
	2015 Oct 23	18.57	19.42	314.1	DES
	2015 Nov 07	18.73	19.40	314.2	DES
	2016 Aug 26	18.21	19.09	318.3	DES
	2016 Sep 22	18.06	19.06	318.6	DES
	2019 Sep 28	17.16	18.13	335.0	OASI
	2019 Nov 30	17.45	18.09	336.0	OASI
	2021 Jan 16	17.89	17.87	342.5	OASI
52007	2016 Aug 08	2.90	3.45	323.3	IAC
	2016 Sep 03	2.59	3.42	327.6	IAC
	2016 Oct 30	2.46	3.37	337.5	IAC
52872	2011 Apr 14	6.37	7.22	81.2	VLT
54598	2020 Sep 13	14.20	14.28	302.4	OASI
	2021 Jan 16	13.49	14.19	304.9	OASI
55576	2003 Mar 09	14.33	15.19	1.0	VLT
60558	2016 Sep 12	5.43	6.30	40.9	VLT
	2016 Oct 04	5.35	6.34	42.5	VLT
	2016 Nov 07	5.50	6.40	44.8	DES
63252	2001 Feb 25	7.13	7.87	63.0	VLT
70032	2017 Aug 22	3.95	4.62	190.9	DES
	2017 Sep 14	3.71	4.60	192.8	DES
	2017 Oct 12	3.59	4.58	195.1	DES
83982	2007 Jul 14	14.01	14.74	37.9	VLT
85490	2007 Apr 18	5.27	5.69	162.5	VLT
87555	2013 Sep 29	26.28	27.27	102.9	DES
	2013 Oct 28	26.54	27.33	103.1	DES
	2016 Sep 22	28.34	29.34	109.8	DES
90572	2013 Sep 28	3.07	3.83	113.8	DES
	2013 Oct 02	3.04	3.84	114.3	DES
	2013 Nov 13	2.98	3.93	119.4	DES

Table A.1. continued.

Object	Date	Δ (au)	r (au)	f (deg)	Observatory[1]
	2013 Dec 01	3.11	3.96	121.5	DES
	2019 Aug 23	1.92	2.92	44.3	OASI
	2019 Sep 03	1.97	2.94	46.6	OASI
	2020 Sep 13	3.12	3.76	109.3	OASI
95626	2004 Mar 24	19.65	20.61	288.6	VLT
118624	2021 Mar 09	4.33	3.79	306.6	OASI
119039	2014 Aug 18	4.54	5.24	153.3	DES
	2014 Nov 18	4.63	5.31	159.9	DES
	2020 May 29	2.43	3.32	10.9	OASI
120061	2008 Feb 04	10.94	11.08	16.8	VLT
145485	2015 Nov 03	1.55	2.43	42.6	IAC
	2015 Dec 04	1.59	2.54	51.6	IAC
145486	2010 Nov 30	7.71	8.29	7.9	VLT
145627	2020 Sep 22	6.39	7.02	233.3	OASI
187661	2017 Oct 16	17.60	17.74	71.1	DES
	2018 Sep 15	17.63	18.24	75.4	DES
196256	2007 Sep 05	2.99	3.46	224.4	VLT
	2007 Sep 21	3.11	3.37	226.2	VLT
210718	2014 Oct 03	1.84	2.82	287.3	DES
	2014 Nov 15	1.83	2.67	297.2	DES
	2014 Dec 10	2.01	2.59	303.5	DES
237838	2016 Sep 26	3.85	4.84	229.7	DES
248590	2016 Jan 11	1.35	1.45	272.2	DES
	2016 Feb 12	1.09	1.14	296.4	DES
	2020 Oct 10	1.55	2.21	242.4	OASI
250112	2008 Sep 21	7.80	8.65	349.9	VLT
275618	2021 Mar 09	1.90	2.70	316.5	OASI
281371	2008 Sep 20	10.97	11.69	297.4	VLT
322713	2019 Nov 20	1.42	2.32	93.8	OASI
322966	2017 Oct 21	1.40	2.05	95.3	DES
323137	2021 Mar 09	2.65	3.56	322.2	OASI
332685	2015 Sep 02	6.82	7.69	43.5	DES
	2016 Oct 01	7.52	8.45	62.8	DES
	2016 Nov 07	7.70	8.53	64.4	DES
	2017 Oct 31	8.39	9.34	78.5	DES
	2017 Nov 15	8.48	9.37	79.1	DES
	2018 Jan 05	9.20	9.49	80.9	DES
347784	2014 Sep 04	2.15	3.02	110.3	DES
349933	2020 May 29	6.21	7.11	42.9	DES
366186	2020 Aug 21	1.81	2.63	37.4	OASI
371522	2014 Aug 19	3.82	4.50	293.7	DES
	2014 Sep 16	3.58	4.48	296.7	DES
406803	2020 Aug 21	1.62	2.61	264.7	OASI
459971	2016 Sep 09	7.06	8.00	76.7	DES
	2016 Oct 01	7.07	8.07	77.7	DES
	2016 Nov 25	7.69	8.24	80.1	DES
465293	2013 Sep 10	2.97	3.92	236.1	DES
471339	2014 Oct 14	9.53	10.40	305.0	DES
472265	2013 Sep 02	9.70	10.63	332.4	DES
	2014 Oct 21	9.48	10.40	346.1	DES
	2014 Nov 13	9.60	10.40	346.7	DES
487496	2014 Oct 02	2.45	3.43	7.8	DES
	2014 Nov 03	2.51	3.44	13.5	DES
494667	2016 Jul 07	1.11	1.70	333.8	IAC
	2016 Oct 03	0.86	1.70	24.3	IAC
499522	2019 Sep 28	19.18	20.18	254.4	OASI
501585	2019 Nov 20	4.29	5.00	30.5	OASI
503273	2017 Aug 28	6.24	7.04	326.1	DES
	2017 Oct 22	6.00	6.96	329.6	DES
	2019 Nov 21	5.84	6.81	22.8	OASI
504160	2016 Aug 26	4.57	5.31	235.9	DES

Table A.1. continued.

Object	Date	Δ (au)	r (au)	f (deg)	Observatory[1]
	2016 Nov 05	4.18	5.05	241.0	DES
515718	2014 Oct 23	3.18	4.17	302.4	DES
	2014 Nov 21	3.26	4.13	305.9	DES
523673	2019 Sep 03	18.86	19.85	291.1	OASI
523710	2016 Aug 25	17.97	18.96	345.4	DES
	2016 Sep 26	18.14	18.95	345.9	DES
	2016 Nov 06	18.67	18.93	346.5	DES
523720	2019 Aug 23	15.93	16.93	333.4	OASI
523727	2019 Aug 23	22.26	23.21	238.7	OASI
523729	2014 Oct 03	11.05	12.03	349.9	DES
523734	2017 Dec 07	18.33	18.87	350.6	DES
523739	2018 Nov 28	11.01	11.24	51.8	DES
523797	2017 Sep 27	10.19	11.09	27.2	DES
	2017 Oct 21	10.50	11.13	28.1	DES
	2018 Sep 29	11.00	11.77	39.5	DES
527443	2008 Sep 21	10.20	11.16	86.3	VLT
	2014 Sep 30	14.06	14.63	130.7	DES
	2014 Oct 31	13.88	14.67	131.2	DES
	2014 Nov 21	13.89	14.70	131.5	DES
	2015 Dec 15	14.46	15.18	137.5	DES
540205	2017 Nov 10	2.96	3.60	326.8	DES
	2017 Dec 14	3.07	3.54	332.7	DES
576357	2016 Sep 26	17.05	17.84	326.9	DES
	2017 Sep 27	16.76	17.59	332.7	DES
	2017 Oct 22	17.04	17.57	333.1	DES
	2018 Nov 26	17.28	17.36	339.5	DES
584778	2016 Oct 28	6.95	7.25	343.2	DES
	2017 Sep 27	6.29	7.13	6.9	DES
	2017 Oct 22	6.47	7.15	8.7	DES
	2019 Aug 24	7.77	8.57	50.1	OASI
601690	2014 Oct 15	18.22	18.85	354.0	DES
606187	2016 Sep 26	5.50	6.49	298.7	DES
	2016 Oct 05	5.51	6.45	299.3	DES
606653	2016 Sep 24	8.51	9.17	305.8	DES
	2016 Oct 02	8.57	9.15	306.1	DES
612093	2016 Sep 24	8.63	9.34	226.9	DES
	2016 Dec 31	8.84	9.11	229.8	DES
	2017 Aug 30	7.91	8.49	237.6	DES
	2017 Dec 07	7.79	8.22	241.1	DES
	2018 Nov 29	6.86	7.17	256.0	DES
	2019 Aug 24	5.45	6.33	270.6	OASI
612530	2013 Sep 29	3.40	4.33	214.4	DES
613349	2021 Mar 09	2.29	3.06	349.6	OASI
644262	2020 Aug 21	2.09	3.09	311.3	OASI
661762	2021 Apr 07	2.83	3.41	46.3	OASI
670321	2018 Oct 19	17.60	18.56	308.3	DES
693675	2016 Sep 11	2.22	2.97	13.2	DES
737875	2017 Aug 17	1.80	2.71	72.2	DES
	2017 Sep 08	1.92	2.79	77.2	DES
2000 CN$_{152}$	2017 Oct 29	4.01	4.87	99.5	DES
2000 XO$_8$	2017 Oct 22	0.50	1.48	6.4	DES
2004 RT$_{109}$	2018 Sep 17	0.68	1.67	347.1	DES
	2018 Nov 30	1.23	1.73	28.6	DES
2005 CR$_{16}$	2020 Dec 19	2.70	3.48	323.2	OASI
2005 XR$_{132}$	2021 Mar 09	1.39	2.27	36.9	OASI
2007 UL$_{147}$	2016 Aug 15	2.41	3.17	315.3	DES
	2016 Sep 09	2.17	3.12	320.3	DES
	2016 Oct 01	2.08	3.08	324.7	DES
	2016 Nov 19	2.35	3.02	334.9	DES
	2016 Dec 05	2.53	3.00	338.4	DES
2007 VH$_{305}$	2008 Nov 22	7.85	8.64	330.4	VLT

Table A.1. continued.

Object	Date	Δ (au)	r (au)	f (deg)	Observatory[1]
2009 UA$_{17}$	2018 Sep 10	2.50	3.47	272.0	DES
	2018 Oct 01	2.39	3.38	275.4	DES
2009 VD$_{78}$	2017 Sep 25	3.06	3.48	316.3	DES
	2017 Oct 17	3.26	3.45	319.9	DES
	2018 Nov 15	2.51	3.38	31.2	DES
2010 ER$_{22}$	2021 Jan 18	1.73	2.64	49.3	OASI
2010 RP$_{80}$	2015 Aug 18	0.57	1.57	287.9	DES
2011 LA$_{19}$	2016 Nov 18	0.95	1.57	84.0	DES
2012 PD$_{26}$	2013 Sep 08	10.64	11.65	52.7	DES
2013 NS$_{11}$	2015 Jan 14	2.48	2.88	31.2	DES
2013 RN$_{30}$	2013 Sep 30	7.28	8.24	342.1	DES
2014 OG$_{392}$	2018 Nov 27	9.85	10.28	323.1	DES
2014 SS$_{303}$	2014 Aug 18	5.97	6.76	0.9	DES
2014 TK$_{34}$	2014 Aug 18	4.28	4.89	308.9	DES
2014 VF$_{40}$	2014 Sep 20	2.27	2.86	293.6	DES
	2014 Nov 02	1.85	2.70	304.5	DES
	2014 Dec 11	1.84	2.58	314.7	DES
2014 WY$_{359}$	2014 Sep 24	2.48	3.33	295.5	DES
	2014 Oct 29	2.24	3.21	302.0	DES
2015 BK$_{22}$	2020 Sep 15	1.38	2.23	347.5	OASI
	2020 Oct 09	1.32	2.22	356.3	OASI
	2021 Jan 16	2.06	2.31	30.1	OASI
2015 BV$_{512}$	2014 Nov 18	1.22	1.33	345.8	DES
2015 BW$_{524}$	2015 Jan 03	5.04	5.71	290.7	DES
2015 PJ$_{311}$	2018 Dec 01	8.67	9.51	72.2	DES
2015 PO$_{324}$	2015 Oct 08	1.60	2.57	6.3	DES
	2015 Dec 28	2.18	2.66	28.6	DES
2015 RK$_{245}$	2015 Sep 30	2.08	3.07	322.1	DES
2015 RR$_{235}$	2015 Dec 05	1.84	2.64	71.8	DES
2015 TN$_{178}$	2016 Feb 06	3.39	3.23	298.3	DES
2015 TS$_{350}$	2014 Nov 14	5.04	5.52	33.9	DES
	2016 Jan 12	7.17	7.26	67.6	DES
2015 UH$_{67}$	2015 Sep 04	5.96	6.66	0.5	DES
	2015 Oct 17	5.68	6.66	3.1	DES
	2015 Nov 06	5.73	6.67	4.3	DES
2015 VA$_{53}$	2015 Sep 23	1.78	2.68	72.3	DES
	2015 Oct 04	1.81	2.74	74.9	DES
	2015 Nov 16	2.25	3.00	84.1	DES
2015 VV$_{1}$	2014 Sep 04	7.85	8.37	19.3	DES
	2014 Nov 25	7.61	8.46	23.5	DES
2015 XX$_{351}$	2016 Nov 07	1.79	2.62	53.9	DES
2015 YY$_{18}$	2016 Dec 05	3.71	4.51	66.1	DES
2016 BJ$_{81}$	2018 Mar 12	4.80	5.51	45.9	DES
2016 ED$_{85}$	2020 Aug 22	0.58	1.46	275.4	OASI
	2020 Sep 14	0.31	1.24	291.0	OASI
2016 KX$_{4}$	2017 Oct 14	1.92	2.67	50.7	DES
	2017 Nov 18	2.04	2.85	59.6	DES
2016 NG$_{39}$	2017 Dec 14	3.01	3.72	107.9	DES
	2018 Jan 17	3.44	3.92	111.8	DES
2016 NX	2016 Sep 12	0.44	1.36	34.1	DES
2016 PM$_{1}$	2016 Aug 26	1.44	2.28	88.4	DES
	2016 Oct 22	1.89	2.64	102.6	DES
2016 PN$_{66}$	2016 Oct 25	1.99	2.90	3.0	DES
	2016 Dec 19	2.72	2.97	17.9	DES
2016 US$_{109}$	2016 Nov 30	1.10	1.96	26.0	VLT
	2017 Feb 03	2.13	2.31	53.4	DES
2016 VF$_{1}$	2014 Dec 15	7.17	7.49	291.3	DES
2016 WP$_{51}$	2016 Sep 09	1.47	2.25	353.2	DES
2016 YB$_{13}$	2017 Sep 25	2.53	3.25	10.4	DES
2017 MZ$_{4}$	2017 Aug 16	2.25	3.25	16.5	VLT
2017 RJ$_{16}$	2017 Oct 11	0.55	1.49	329.2	DES

Table A.1. continued.

Object	Date	Δ (au)	r (au)	f (deg)	Observatory[1]
2017 WW$_{14}$	2016 Sep 09	5.31	6.26	324.8	DES
	2016 Nov 18	5.46	6.10	330.5	DES
2017 YL$_2$	2016 Nov 10	3.41	4.29	259.3	DES
2018 AS$_{18}$	2018 Aug 26	2.27	2.58	76.6	VLT
2018 LN$_6$	2018 Oct 19	1.04	2.03	69.2	DES
	2018 Nov 06	1.20	2.13	75.6	DES
2019 KN$_{19}$	2020 Aug 21	2.10	3.09	29.7	OASI
2019 UH$_{12}$	2018 Sep 11	7.20	7.91	0.7	DES
2019 WV$_2$	2018 Nov 29	4.30	4.70	275.2	DES

Table A.2. Observational information for AAs.

Object	Date	Δ (au)	r (au)	f (deg)	Observatory[1]
133P	2007 Jul 13	1.63	2.64	3.3	VLT
	2019 Aug 24	2.25	2.97	76.0	OASI
259P	2017 Sep 25	1.13	1.85	24.0	DES
311P	2013 Sep 29	1.16	2.09	287.2	DES
	2013 Oct 12	1.23	2.07	291.5	DES
	2013 Nov 9	1.46	2.04	301.1	DES
	2016 Jun 8	1.60	2.34	228.4	VLT
324P	2015 Apr 18	2.55	2.77	305.8	VLT
331P	2015 Dec 15	2.90	1.95	37.1	VLT
	2017 Mar 27	2.21	3.07	126.2	DES
354P	2019 Aug 24	1.57	2.23	275.4	OASI
P/2015 X$_6$	2015 Nov 18	1.43	2.36	323.3	DES

---

[1] Observations from OASI and IAC were conducted using an R filter. Selected VLT images were obtained with VRI filters. Finally, DES images were acquired using grizY filters.